Development of a discontinuous Galerkin ionosphere-plasmasphere model

Houjun Wang

CIRES, University of Colorado at Boulder, Colorado, USA

Key Points:

- The high-order discontinuous Galerkin (DG) method is used to solve the multi-fluid plasma dynamical equations along the magnetic field line
- Converging results of simulations with different element size and polynomial order indicate robustness of algorithms and implementation
- The model algorithms also capture the dawn terminator effect very well in the He^+ density field

Corresponding author: Houjun Wang, Houjun.Wang@colorado.edu

Abstract

The objective of this study is to explore the application of high-order numerical methods in ionosphere-plasmasphere modeling. Specifically, the nodal discontinuous Galerkin (DG) method is chosen to solve the multifluid dynamical equations along the magnetic field lines. A general curvilinear magnetic field-line-following coordinate system is also used in the model. Numerical simulations with different combinations of number of elements (K) and polynomial orders (N) show the *converging* results, indicating the robustness of the algorithms and implementation. The model also captures the dawn terminator effect very well in the He^+ field.

1 Introduction

The Earth's ionosphere and plasmasphere is a multi-fluid system involving complex physical-chemical and electrodynamic processes that span many orders of magnitude changes. This complexity presents a great challenge to numerical methods for accurate simulation of the ionosphere-plasmasphere system.

Many ionospheric models use the finite-difference methods of at most second-order accuracy with the central difference scheme (e.g., R. W. Schunk, 1996). Some ionospheric models use only approximated equations, e.g., the time-dependent inertial terms are ignored in the momentum equation (e.g., Bailey & Balan, 1996). A good assessment on some of the ionospheric models used at that time was given by Huba et al. (2000). The SAMI2 model (Huba et al., 2000) uses the upwind differencing scheme, or the donor cell method, which is conservative but highly diffusive and only first-order accurate. Some newer ionospheric models (e.g., Zettergren & Semeter, 2012) are also using the low-order numerical methods. However, it should be noted that the SAMI3 model uses the high-order interpolation scheme in conjunction with partial donor cell method (Hain, 1987; Huba, 2003). The high-order schemes are used to avoid the excessive numerical diffusion of the low-order methods and to allow steeper density gradients to develop in irregularity simulation (Huba & Liu, 2020).

The advance of high-order numerical methods, such as the spectral element (SE) or discontinuous Galerkin (DG) methods, provides a great opportunity to meet the challenge in modeling the complex multi-scale processes of the ionosphere-plasmasphere system. As defined in Gustafsson (2008), the high-order methods refer to those methods whose order of accuracy $p \geq 3$. Here the order of accuracy p is defined in such a way that the truncation error is proportional to h^p, with h as the discretization step size. The high-order methods are advantageous for solving the wave propagation problems and/or when more accurate solutions of problems are required (e.g, Gustafsson, 2008). High-order spectral methods also have significantly lower phase errors compared to the finite-difference methods (e.g., Canuto et al., 2006). As discussed in Hesthaven (2018), the motivation for development of high-order accurate schemes is "to do more with less, i.e., to develop schemes that are more accurate than first order accurate schemes without substantially increasing the computational cost."

The main advantages of the DG methods over classical finite volume and finite difference methods are (Cockburn et al., 2000):

- Arbitrarily high formal order of accuracy can be obtained by suitably choosing the degree of the approximating polynomials
- Highly parallelizable
- Suitable to handle complicated geometries and simple in treating boundary conditions
- Easy in handling adaptivity

In this study, we explore the applications of the DG methods in ionosphere-plasmasphere modeling. We develop a new ionosphere-plasmasphere model using the DG methods to solve the dynamics and diffusion equations along the geomagnetic field lines. The splitting method is used to solve the ionosphere-plasmasphere model equations sequentially. First, the Euler equations with gravity along the field lines are solved using the DG method for spatial discretization and the strong stability preserving Runge-Kutta method (SSP-RK) for time integration with adaptive time stepping. Then, the thermal diffusion equations for ions and electrons along the field lines are solved using the DG method and Crank-Nicolson (CN) implicit time stepping. Various physical-chemical forcing, including photoionization, chemical productions and losses, collisions, and heating and cooling terms, are then added using a positive-definite ordinary differential equation (ODE) solver. The perpendicular ExB transport is done using a simple semi-Lagrangian (SL) transport scheme, with specified ExB drift velocity mimic empirical ExB drift model.

In addition to the DG methods used in the model, several other new features are introduced in the model. The *ragged array* with variable array length/size along the field lines is used in the model. This approach is very suitable to the ionosphere-plasmasphere modeling considering the varying length of magnetic field lines. It does not involve complicated derived data types (DDT) and saves both computing memory and disk space storage. Another feature is that the native MPI-IO is used for model input and output. This approach is simple and efficient, which works very well with the simple decomposition that divides the model domain into meridional sections/slabs along the geomagnetic longitudes for the MPI tasks. And finally, a new general curvilinear field-line-following coordinate system (Wang, 2021) is also used in the model.

This paper is organized as follows. In the next section, we describe various aspects of the DG model: the nodal DG method for the field-aligned dynamics and diffusion, the physical-chemical forcing ODE solver, the perpendicular ExB transport, and some aspects of the model code. In section 3, we present results of model simulations using different combinations of number of elements (K) and polynomial orders (N), showing the converging results of the total electron content (TEC) and model's ability to capture the terminator effect. And a summary is given in section 4. Some mathematical details related to the DG methods, such as limiter and filter, and computation of physical forcing terms are given in the Appendix.

2 The discontinuous Galerkin (DG) ionosphere-plasmasphere model

2.1 The model equations along the field line and overview of the model

The ionosphere and plasmasphere are modeled as a multi-fluid system. In the general curvilinear magnetic field-line-following coordinate system $(\mu, \chi, \phi) \Rightarrow (\mu_m, \chi_m, \phi_m)$ (Wang, 2021), the one-dimensional Euler equations with gravity can be written as

$$\frac{\partial \rho_i}{\partial t} + \frac{1}{h_\mu h_\chi h_\phi}\frac{\partial}{\partial \mu}[h_\chi h_\phi (\rho_i u_i)] = 0, \tag{1a}$$

$$\frac{\partial \rho_i u_i}{\partial t} + \frac{1}{h_\mu h_\chi h_\phi}\frac{\partial}{\partial \mu}[h_\chi h_\phi (p_i + \rho_i u_i^2)] = -\rho_i g_{\shortparallel}, \tag{1b}$$

$$\frac{\partial E_i}{\partial t} + \frac{1}{h_\mu h_\chi h_\phi}\frac{\partial}{\partial \mu}[h_\chi h_\phi (E_i + p_i) u_i] = -\rho_i u_i g_{\shortparallel}, \tag{1c}$$

where ρ_i is density, $\rho_i u_i$ is the momentum, E_i is the energy (internal and kinetic) per unit volume, with the subscript i denoting the different ion species; h_μ, h_χ, h_ϕ are the scale factors; and $g_{\shortparallel}$ is gravity parallel to the field line. The pressure is related to the energy through the ideal gas law as

$$p_i = (\gamma_i - 1)\left(E_i - \frac{1}{2}\rho_i u_i\right), \quad c_i = \sqrt{\frac{\gamma_i p_i}{\rho_i}},$$

where c_i is the local speed of sound and γ_i is the specific heat ratio. The advantage of using the set of equations in this conservative form is shown by Giraldo & Restelli (2008). Using the spectral element (SE) and discontinuous Galerkin (DG) methods, they demonstrated that numerical solutions are less dissipative when the equation set is written in this form than in other forms discussed in their paper.

The set of equations of (1) excludes the diffusion and physical-chemical forcing terms, which will be described in section 2.3 and 2.4, respectively. The perpendicular ExB drift is discussed in section 2.5

Ideally, various physical-chemical source terms should be added to the dynamical solver and treated seamlessly together in just one setting. Currently, we split the computation into dynamics/advection, diffusion and physical-chemical forcing steps. As will be discussed shortly, the dynamics/advection step is solved *explicitly* using the DG method for spatial discretization and the strong stability preserving Runge-Kutta method (SSP-RK) for time integration; the diffusion step is solved *implicitly* using the DG method for spatial discretization and the Crank-Nicolson (CN) scheme for time integration; and the physical-chemical forcing part is solved using an unconditionally stable positive-definite scheme. Using the so-called Strang operator splitting (Strang, 1968), the advection-diffusion-chemical ($\mathcal{ADC}$) operators are treated sequentially as follows (e.g, Fazio & Jannelli (2010)):

$$\frac{\partial q}{\partial t} = \mathcal{A}(\delta t/2)\mathcal{D}(\delta t/2)\mathcal{C}(\delta t)\mathcal{D}(\delta t/2)\mathcal{A}(\delta t/2)q,$$

which results in a second-order splitting error. However, this can be expensive. To save time, we can simply use

$$\frac{\partial q}{\partial t} = \mathcal{C}(\delta t)\mathcal{D}(\delta t)\mathcal{A}(\delta t)q,$$

which is used in the simulations discussed in this paper.

2.2 The nodal discontinuous Galerkin methods for field-aligned dynamics

We rewrite the set of equations (1) in the vector form as

$$\frac{\partial \boldsymbol{q}}{\partial t} + \frac{\partial \boldsymbol{F}}{\partial x} = \boldsymbol{G}, \tag{2}$$

where

$$\boldsymbol{q} = \begin{bmatrix} \rho_i \\ \rho_i u_i \\ E_i \end{bmatrix}, \quad \boldsymbol{F} = \begin{bmatrix} h_\chi h_\phi(\rho_i u_i) \\ h_\chi h_\phi(p_i + \rho_i u_i^2) \\ h_\chi h_\phi(E_i + p_i)u_i \end{bmatrix}, \quad \boldsymbol{G} = \begin{bmatrix} 0 \\ -\rho_i g_{\shortparallel} \\ -\rho_i u_i g_{\shortparallel} \end{bmatrix}.$$

The equation system is solved using the nodal discontinuous Galerkin (DG) methods (e.g., Hesthaven & Warburton, 2008).

Approximate the 1D domain $\Omega = [x_L, x_R]$ by K non-overlapping elements $\mathsf{D}^k = [x_l^k, x_r^k]$. On each element, we introduce N_p local grid points, $x_i^k \in \mathsf{D}^k$, usually the Legendre-Gauss-Lobatto (LGL) quadrature points (e.g., Deville et al., 2002; Canuto et al., 2006). In the nodal representation, we express the local solution and the local flux as a polynomial of order $N = N_p - 1$, through the associated interpolating Lagrange polynomial, $\ell_i^k(x)$, as follows:

$$\boldsymbol{q}_h^k(x,t) = \sum_{i=1}^{N_p} \boldsymbol{q}_h^k(x_i^k,t)\ell_i^k(x), \quad \boldsymbol{F}_h^k(\boldsymbol{q}_h^k(x,t)) = \sum_{i=1}^{N_p} \boldsymbol{F}_h^k(x_i^k,t)\ell_i^k(x),$$

and similarly for the right-hand side term. The nodal values $\boldsymbol{q}_h^k(x_i^k,t)$ are the unknowns. Then on each element, we require that the residual is orthogonal to the test function, which is the same as the basis function for the Galerkin method,

$$\int_{\mathsf{D}^k} \left(\frac{\partial \boldsymbol{q}_h^k}{\partial t} + \frac{\partial \boldsymbol{F}_h^k}{\partial x} - \boldsymbol{G}_h^k \right) \ell_j^k(x) dx = 0.$$

Interpolation by parts yields

$$\int_{\mathsf{D}^k} \left(\frac{\partial \boldsymbol{q}_h^k}{\partial t} \ell_j^k - \boldsymbol{F}_h^k \frac{d\ell_j^k}{dx} - \boldsymbol{G}_h^k \ell_j^k \right) dx = -[\boldsymbol{F}_h^k \ell_j^k]_{x_l^k}^{x_r^k}.$$

The main purpose of the right-hand side is to connect the neighboring elements. A numerical flux $\boldsymbol{F}^*$ is introduced as a unique value to be used at the element interface. The numerical flux is obtained by combining information from neighboring elements and should appropriately reflect the underling dynamics of the problem.

With this we obtain the DG scheme for the conservation laws in *weak form* as

$$\int_{\mathsf{D}^k} \left(\frac{\partial \boldsymbol{q}_h^k}{\partial t} \ell_j^k - \boldsymbol{F}_h^k \frac{d\ell_j^k}{dx} - \boldsymbol{G}_h^k \ell_j^k \right) dx = -[\boldsymbol{F}^* \ell_j^k]_{x_l^k}^{x_r^k}.$$

Integration by parts once more, we get the DG scheme in *strong form* as

$$\int_{\mathsf{D}^k} \left(\frac{\partial \boldsymbol{q}_h^k}{\partial t} + \frac{\partial \boldsymbol{F}_h^k}{\partial x} - \boldsymbol{G}_h^k \right) \ell_j^k(x) dx = [(\boldsymbol{F}_h^k - \boldsymbol{F}^*) \ell_j^k]_{x_l^k}^{x_r^k}.$$

In matrix form this can be written as

$$\mathcal{M}^k \frac{d}{dt} \boldsymbol{q}_h^k + \mathcal{S}\, \boldsymbol{F}_h^k - \mathcal{M}^k \boldsymbol{G}_h^k = \left[\boldsymbol{\ell}^k(x) (\boldsymbol{F}_h^k - \boldsymbol{F}^*) \right]_{x_l^k}^{x_r^k},$$

where we have introduced the local mass and stiffness matrices:

$$\mathcal{M}_{ij}^k = \int_{\mathsf{D}^k} \ell_i^k(x) \ell_j^k(x) dx, \quad \mathcal{S}_{ij}^k = \int_{\mathsf{D}^k} \ell_i^k(x) \frac{d\ell_j^k}{dx} dx.$$

For the numerical flux $\boldsymbol{F}^*$, we use the monotone Lax-Friedrichs flux:

$$\boldsymbol{F}^*(\boldsymbol{q}_h^-, \boldsymbol{q}_h^+) = \{\{\boldsymbol{F}_h(\boldsymbol{q}_h)\}\} + \frac{C}{2} [\![\boldsymbol{q}_h]\!],$$

where $C = \max |\boldsymbol{F}_{\boldsymbol{q}}|$ is an upper bound on the (local) wave speed. The average $\{\{\cdot\}\}$ and the jump $[\![\cdot]\!]$ (along a cell interface with normal $\mathbf{n}$) are defined as

$$\{\{u\}\} = (u^- + u^+)/2, \quad [\![u]\!] = \mathbf{n}^- u^- + \mathbf{n}^+ u^+,$$

where the superscripts "$-$" and "$+$" refer to the interior and exterior values at the cell interface, respectively.

For time integration we use the strong stability preserving Runge-Kutta method (SSP-RK) (e.g., Gottlieb et al., 2001; Hesthaven & Warburton, 2008), such that no instability would be introduced by time integration if the Courant-Friedrichs-Lewy (CFL) criteria (Courant et al., 1967) are satisfied. The semidiscrete equation

$$\frac{du_h}{dt} = \mathcal{L}_h(u_h, t)$$

is solved using the optimal third-order three-stage SSP-RK scheme as follows

$$\begin{aligned}
v^{(1)} &= u_h^n + \Delta t \mathcal{L}_h(u_h^n, t^n), \\
v^{(2)} &= \frac{1}{4} \left(3u_h^n + v^{(1)} + \Delta t \mathcal{L}_h(v^{(1)}, t^n + \Delta t) \right), \\
u_h^{n+1} &= v^{(3)} = \frac{1}{3} \left(u_h^n + 2v^{(2)} + 2\Delta t \mathcal{L}_h \left(v^{(2)}, t^n + \frac{1}{2} \Delta t \right) \right).
\end{aligned}$$

The slope limiter is applied on the characteristic variables after each time step, see Appendix A for details.

2.3 Discontinuous Galerkin for diffusion

The one-dimensional thermal diffusion equation for ions and electrons along the magnetic field line can be written, with the scale factors, as

$$\frac{\partial T}{\partial t} = \frac{2}{3}\frac{1}{nk_B}\frac{1}{h_\chi h_\phi}\frac{\partial}{h_\mu \partial \mu}\left(h_\chi h_\phi \kappa \frac{\partial T}{h_\mu \partial \mu}\right), \tag{3}$$

where $T = T_{i,e}$ is the temperature, $n = n_{i,e}$ is the number density and $\kappa = \kappa_{i,e}$ is the diffusion coefficient, with the subscripts i and e denoting ion and electron, respectively; and k_B is the Boltzmann constant. Expressions for computing thermal conductivities are given in Appendix B1. Write the diffusion equation (3) in the form

$$\frac{\partial T}{\partial t} = b\frac{\partial}{\partial x}\left(a\frac{\partial T}{\partial x}\right),$$

and then rewrite it as a system of the first-order equations

$$\frac{\partial T}{\partial t} = b\frac{\partial}{\partial x}\left(\sqrt{a}q\right), \quad q = \sqrt{a}\frac{\partial T}{\partial x}, \tag{4}$$

which is what to be solved using the DG methods.

The DG discretization of the system of equations (4) can be written in matrix form as

$$\mathcal{M}^k \frac{d\mathbf{T}_h^k}{dt} = \mathcal{B}^k \mathcal{S}^k \mathcal{A}^k \mathbf{q}_h^k - \left[\boldsymbol{\ell}^k(x)((b\sqrt{a}q_h^k) - (b\sqrt{a}q_h^k)^*)\right]_{x_l^k}^{x_r^k}, \tag{5a}$$

$$\mathcal{M}^k \mathbf{q}_h^k = \mathcal{A}^k \mathcal{S}^k \mathbf{T}_h^k - \left[\boldsymbol{\ell}^k(x)((\sqrt{a}T_h^k) - (\sqrt{a}T_h^k)^*)\right]_{x_l^k}^{x_r^k}, \tag{5b}$$

where $\mathcal{A}_{ii}^k = \sqrt{a(x_i^k)}$ and $\mathcal{B}_{ii}^k = b(x_i^k)$ The numerical flux are chosen as follows:

$$(b\sqrt{a}q_h^k)^* = \{\{b\sqrt{a}q_h^k\}\} - \tau[\![abu_h^k]\!], \quad (\sqrt{a}T_h^k)^* = \{\{\sqrt{a}T_h^k\}\},$$

with an interior penalty τ term to disallow large jumps at the element interface and to stabilize the solution. The penalty parameter, or the stabilization parameter, τ, is chosen such that (Shahbazi, 2005; Hesthaven & Warburton, 2008)

$$\tau \geq c_\tau N_p^2/h, \quad c_\tau \geq 1/2,$$

where h is the element size. We use $c_\tau = 3/2$ in all simulations discussed in this paper.

For the time integration of the diffusion equation, we write the diffusion equation after the DG discretization (5) in the semidiscrete form as

$$\frac{dT_h}{dt} = \mathbb{H}T_h,$$

and then use the second-order implicit Crank-Nicolson (CN) scheme for time discretization as

$$\frac{T_h^{n+1} - T_h^n}{\Delta t} = \frac{1}{2}(\mathbb{H}T_h^{n+1} + \mathbb{H}T_h^n),$$

or

$$\left(\mathbb{I} - \frac{1}{2}\Delta t\mathbb{H}\right)T_h^{n+1} = \left(\mathbb{I} + \frac{1}{2}\Delta t\mathbb{H}\right)T_h^n,$$

which is to be solved using the LAPACK's linear solver 'dgbsv' for the system of linear equations with the general banded matrix (Anderson et al., 1999). The exponential filter is then used. It should be noted that the DG for diffusion with large varying diffusivity is indeed a challenging problem (e.g., Proft & Rivière, 2009). The combination of the DG discretization with the interior penalty term and filtering seems to work well.

2.4 Adding the physical-chemical forcing terms

Various physical-chemical source terms appear in the equations of the ionosphere-plasmasphere model. As discussed above, we use the operator splitting scheme in this study. The physical-chemical source terms are added to the model by solving the following set of ordinary differential equations (ODEs):

$$\frac{dn_i}{dt} = P_i - n_i L_i, \tag{6a}$$

$$\frac{du_i}{dt} = -\nu_{in}(u_i - u_n) - \sum_j \nu_{ij}(u_i - u_j), \tag{6b}$$

$$\frac{dT_i}{dt} = Q_{in} + Q_{ii} + Q_{ie}, \tag{6c}$$

$$\frac{dT_e}{dt} = Q_{en} + Q_{ei} + Q_{\mathrm{phe}}, \tag{6d}$$

where P_i and L_i are the ion production and ion loss terms; ν_{in} and ν_{ij} are ion-neutral and ion-ion collision frequencies; and Q_{phe} is the photoelectron heating rate. Other collisional heating terms are given by:

$$Q_{in} = \frac{2}{3}\sum_q \frac{m_i m_q}{(m_i + m_q)^2}\nu_{iq}\left[3(T_q - T_i) + \frac{m_q}{k_B}(u_q - u_i)^2\right], \tag{7a}$$

$$Q_{ii} = \frac{2}{3}\sum_j \frac{3.3\times 10^{-4} n_j}{A_i A_j (T_i/A_i + T_j/A_j)^{3/2}}(T_j - T_i), \tag{7b}$$

$$Q_{ie} = \frac{2}{3}\frac{7.7\times 10^{-6} n_e}{A_i T_e^{3/2}}(T_e - T_i), \tag{7c}$$

$$Q_{en} = \frac{2}{3}\sum_q \frac{m_e m_q}{(m_e + m_q)^2}\nu_{eq}[3(T_q - T_e)], \tag{7d}$$

$$Q_{ei} = \frac{2}{3}\sum_j \frac{7.7\times 10^{-6} n_j}{A_j T_e^{3/2}}(T_j - T_e), \tag{7e}$$

where q denotes summation over neutrals and j summation over ions. The Appendix B gives more details on computation of collision frequency and heating rate and a brief description of a simple photoelectron heating model, but see Huba et al. (2000) for the description of photoionization and chemistry model. The computation of the physical-chemical forcing terms are based on SAMI2 open source code modified for the current model.

The set of ODEs for the physical-chemical forcing can be written in the form of production-destruction equation as follows:

$$\frac{dc_i}{dt} = P_i(\boldsymbol{c}) - D_i(\boldsymbol{c}),$$

where $P_i(\boldsymbol{c}) \geq 0$ and $D_i(\boldsymbol{c}) \geq 0$ represent the production and destruction rates of the ith constituent, respectively. The set of production-destruction equations is solved with the Patankar-Euler integration scheme (Burchard et al., 2003) as

$$c_i^{n+1} = c_i^n + \Delta t\left(P_i(\boldsymbol{c}^n) - D_i(\boldsymbol{c}^n)\frac{c_i^{n+1}}{c_i^n}\right),$$

using the so-called Patankar trick (Patankar, 1980). This is a (unconditionally) positive scheme, i.e., $\boldsymbol{c}^{n+1} > 0$ for any $\boldsymbol{c}^n > 0$ with any time step size $\Delta t \geq 0$.

2.5 The perpendicular transport: ExB drift

Simple vertical and zonal ExB drift velocity profiles that mimic the empirical ExB model (e.g., Scherliess & Fejer, 1999; Fejer et al., 2005) are used in this study, similar

to what is used in the SAMI2 model. The vertical and zonal ExB drift velocities at the magnetic equator are given by

$$v_{\rm exb} = v_0 \sin(2\pi(h_{\rm lt} - 6)/24) + v_{\rm pre} \exp[-(h_{\rm lt} - 19)/\delta_{\rm pre})^2], \tag{8}$$

where $v_0 = 25, v_{\rm pre} = 50$ for vertical drift and $v_0 = -40, v_{\rm pre} = 120$ for zonal drift, $\delta_{\rm pre} = 2$, with the subscript 'pre' denoting the 'pre-reversal enhancement'. The simple ExB drift velocity model gives more flexibilities in model development and testing in terms of adjusting the model parameters.

The algorithm for the ExB drift is implemented in the sense that plasma along each flux tube moves as a whole, taking into account of the effect of flux tube volume change on plasma density and adiabatic effect on temperature. Currently the low-order, non-conservative semi-Lagrangian (SL) scheme is used in the model. In the future, conservative high-order transport schemes, such as the semi-Lagrangian discontinuous Galerkin (SLDG) scheme (e.g., Cai et al., 2017), will be implemented.

2.6 Some aspects of the model code

We should point out a few features of the model's source code. The model uses standard Fortran 90 or later features, without sophisticated data structure or derived data types (DDT). However, the *ragged array* with variable length is used. This is found to be very useful in representing the data of variable length along the geomagnetic field lines, which can save data storage space and/or runtime memories. It can also improve overall model efficiency. Here is an example on using the ragged array:

```
! define an allocatable data type for variable length
type vc1d
   real(dp), allocatable :: vc1d(:)
end type vc1d

! use the data type to define a ragged array
type(vc1d), dimension(:,:), allocatable :: b

! allocate the ragged array with variable length,
!               i.e., klm(l,m) depending on (l,m)
allocate ( b(nlp,nmp) )
do m = 1, nmp
do l = 1, nlp
allocate ( b(l,m)%vc1d( klm(l,m) ) )
enddo
enddo
```

Another feature of the model is that MPI-IO (Gropp et al., 2014) is used for model input and output, which improves model I/O efficiency. This approach appears to be simpler than using other parallel I/O libraries, such as HDF-5 (`https://en.wikipedia.org/wiki/Hierarchical_Data_Format`) or PnetCDF (`https://parallel-netcdf.github.io/`).

3 Numerical simulations and results

We demonstrate the model with three-dimensional simulations using different combinations of number of elements (K) and polynomial orders (N). The first set of simulations uses the same number of elements, but varies the polynomial orders (from N = 2 to 4). The second set of simulations varies both K and N such that the overall resolutions are similar between the simulations.

Table 1. The total number of elements.

	K101	K135	K201
Number of elements	1 147 886	1 545 019	2 315 954

3.1 Model configurations

The number of grid points in the zonal and meridional direction, or the magnetic longitudes and latitudes, is the same for all simulations. We use 225 grid points between magnetic co-latitudes 45° and 82°, and 90 grid points in magnetic longitudes. The grid resolution along the flux tube is determined by the number of points along the *outermost* flux tube between the two foot points where they cross the Earth's surface. Note that the model uses only nodal points whose altitudes are higher than 90 km; see Wang (2021) for details on grid generation and metric coefficients computation.

In this study, three set of model resolutions along the flux tube are used. The numbers of nodal points along the outermost flux tube between the two foot points are 101, 135 and 201, which will be denoted by K101, K135 and K201, respectively, in the following discussion. The corresponding total number of elements for each K-resolution is shown in Table 1,

To demonstrate the implementation of the algorithms described in section 2, we examine simulation results using three different polynomial orders, $N = 2$, 3, 4, which have the corresponding formal order of accuracy of $N_p = N + 1 = 3$, 4, 5. In the first set of runs, the number of elements along the flux tubes is kept the same, K101. In the second set of runs, the number of elements and polynomial order are chosen such that the overall resolutions are about the same along the flux tubes. We have used combinations of K201/N2, K135/N3 and K101/N4 in this set of runs; see Table 2.

The model solves for the ion density, temperature, and the field-aligned velocity and electron temperature. Seven ion species (H^+, He^+, O^+, N^+, NO^+, O_2^+, N_2^+) and seven neutral species (H, He, O, N, NO, O2, N2) are used in the model in the numerical experiments of this study.

Neutral temperature and composition are specified by the Mass Spectrometer and Incoherent Scatter radar (MSIS) model (Hedin, 1987), except nitric oxide, which is not included in the MSIS model. A simple expression of the NO density is used (Mitra, 1968; Bailey & Balan, 1996):

$$n[\mathrm{NO}] = 0.4\exp\big(-3700/T_n\big)n[\mathrm{O_2}] + 5\times10^{-7}n[\mathrm{O}] \quad [\mathrm{cm^{-3}}].$$

The neutral winds are from the Horizontal Wind Model (HWM) (Hedin et al., 1991). The initial conditions for plasmas are generated from the International Reference Ionosphere (IRI) model (Bilitza, 2018). Fixed $F10.7 = 181$ and $Ap = 1$ are used.

As discussed previously, the dynamics, diffusion and physical-chemical forcing are solved sequentially. The time step for diffusion and physics-chemistry is 15 seconds. The time step for the parallel dynamics solver is *adaptive* or sub-time-stepping according to the Courant-Friedrichs-Lewy (CFL) criteria.

The slope limiter is applied to the characteristic variables in the dynamics step and to the primitive variables in the physics-chemistry step. The exponential filter is only used for the ion and electron temperatures in the diffusion step. In all the cases, the smoothness indicator (S_I) is used to choose where to applied the limiter or filter; the same $C_R = 1.0\times10^{-6}$ is used in the smoothness threshold; and the same filter order $s = 6$ is used

Table 2. The relative wallclock time for the simulations.

	K101	K135	K201
N2	0.38		1.37
N3	0.62	1.09	
N4	1.00		

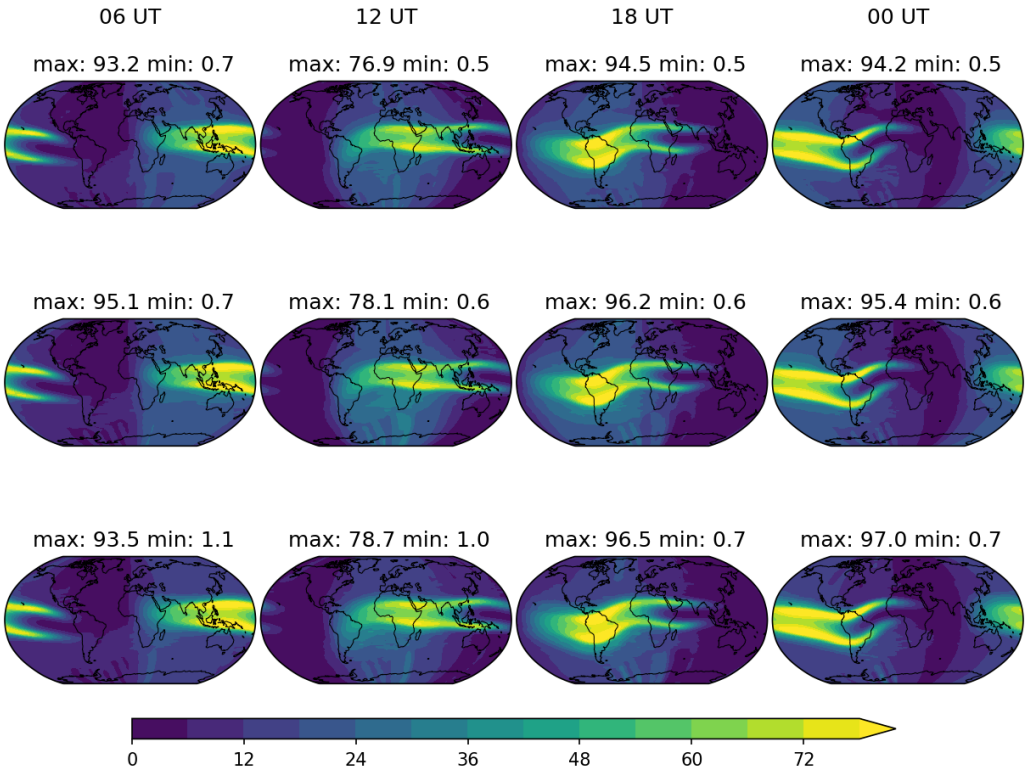

Figure 1. The TEC simulations, using the same number of elements (K101), but varying polynomial orders N: the first row is with N2, the second row with N3, and the third row with N4. Four UT times (06, 12, 18, and 00 UT) are shown, respectively for 6, 12, 18 and 24 hour simulations, initialized at 00 UT on 21 March 2000.

in the exponential filter; see Appendix A for details. These parameters, as well as the polynomial order N, are specified at the run time from the Fortran *namelist* input.

Table 2 shows the relative run/wall-clock time for each simulation. The run time for the second set of simulations (with similar resolutions) show that the higher order simulation uses less time.

3.2 Simulating the total electron content (TEC)

We compare the simulations with different combinations of number of elements (K) and polynomial orders (N). Figure 1 shows the vertically-integrated TEC from the first set of runs which keeps the same number of elements (K101) and varying the polynomial orders (N = 2, 3, 4). Figure 2 shows the vertically-integrated TEC from the second set of runs which varies both the number of elements and the polynomial orders such

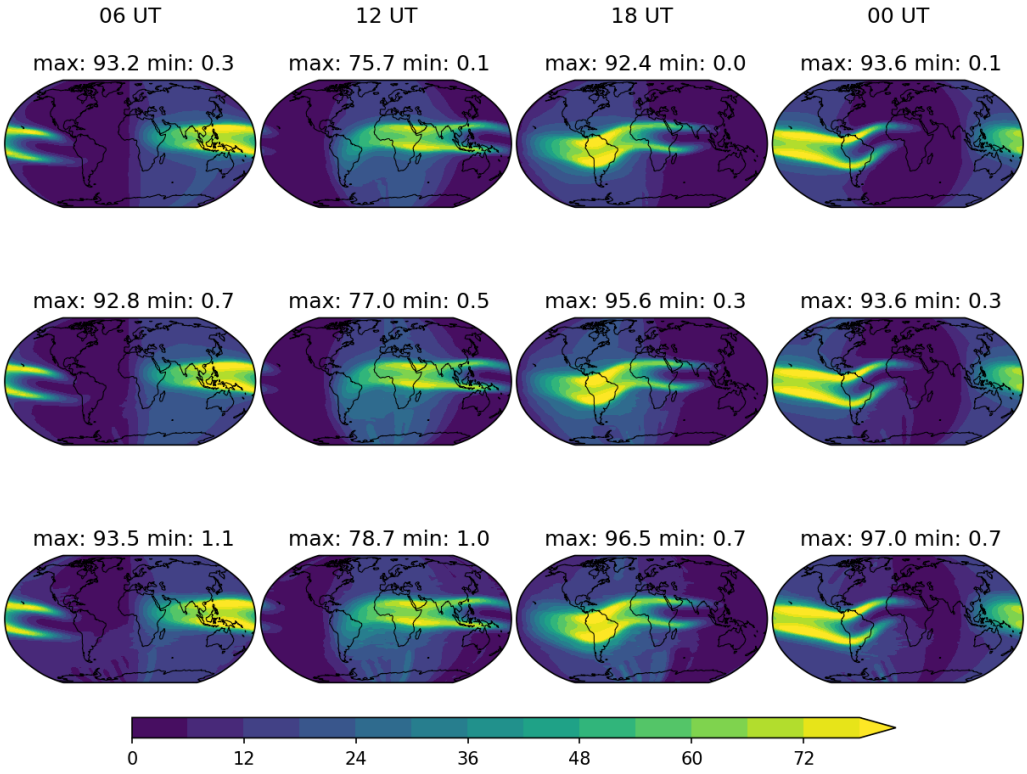

Figure 2. The TEC simulations, using varying number of elements K and varying polynomial orders N: the first row is with K201 and N2, the second row with K135 and N3, and the third row with K101 and N4. Four UT times (06, 12, 18, and 00 UT) are shown, respectively for 6, 12, 18 and 24 hour simulations, initialized at 00 UT on 21 March 2000.

that the overall resolutions are similar. The overall TEC pattern such as the equatorial fountain effect (e.g., R. Schunk & Nagy, 2009) and the east-west movement of TEC are all well simulated. Comparable TECs are obtained with different K/N combinations; the differences of the TEC maxima are less than 5%. The *converging* results of the simulations using different combinations of K/N indicate the robustness of the algorithms and implementation.

The maxima of TEC are slightly higher for runs with higher polynomial order, except for simulations with N3 at 06 UT, possibly because the dynamical DG model has not yet fully spun up from the cold start initialized from the empirical International Reference Ionosphere (IRI) data model. Runs with the higher polynomial order also have slightly higher minima values. These results indicate that the higher order of accuracy (using higher polynomial order) also imply a higher resolving power (resolutions) for model simulations.

3.3 Capturing the terminator effect

An interesting feature of the model is that it can capture very well the terminator effect, i.e., the distinction between before and after the sunrise. The is clearly shown in the He^+ density field (Fig. 3), most noticeably at 14 UT and 15 UT, or at 2 AM and 3 AM local time. The production and loss of He^+ are directly through photoionization with the sunrise and chemical loss during the nighttime (e.g., Denton et al., 2002). This

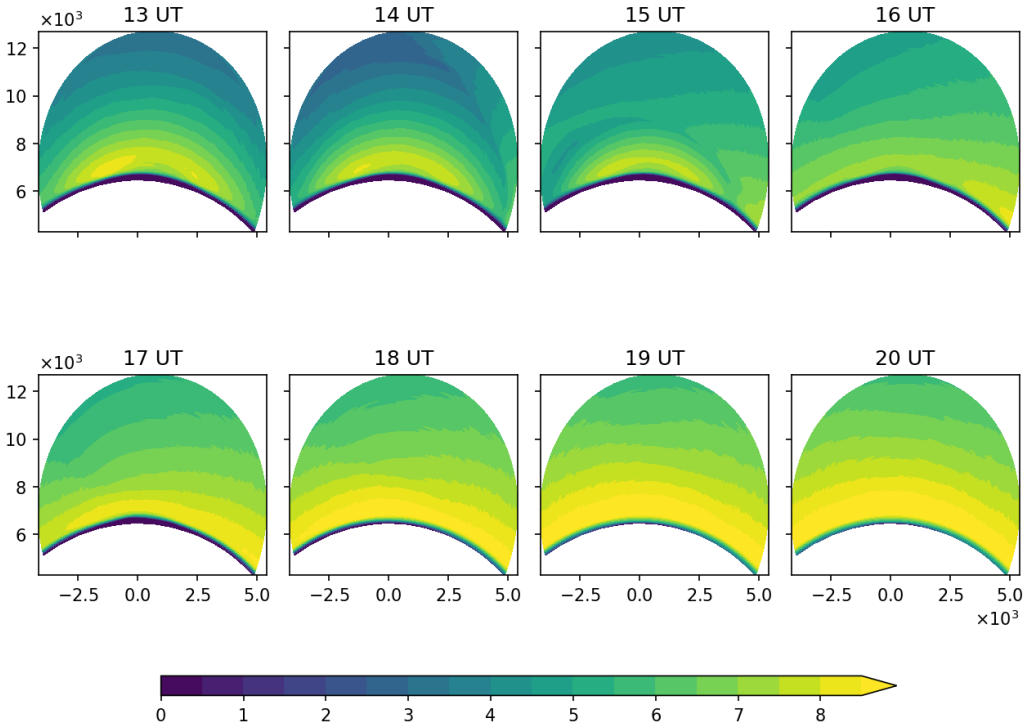

Figure 3. The meridional plane plot of the He^+ density, $\log_{10} n_{He^+}$ [m^{-3}], at the magnetic longitude 180°, showing the dawn terminator effect. The simulation results from the K101/N2 run are shown every hour from 13 to 20 UT, initialized at 00 UT on 21 March 2000. The geocentric x- and y-coordinates in [10^3 km] are used in the plot, with x from north to south.

dawn terminator effect can also potentially affect the formation of the He^+ layer in observations and in modeling (e.g., Wilford et al., 2003).

The model's ability to capture the terminator effect indicates that the effectiveness of the model algorithms in capturing the sharp gradients, which is needed in modeling small scale phenomena such as ionospheric irregularities.

The field-aligned velocity of He^+ (Fig. 4) shows the significant dynamic response of wind to the pressure changes resulting from the ion density changes with the sunrise. However, we don not see such large gradient and dramatic changes in the He^+ ion temperature field, as they are shown in the density and field-line-aligned velocity fields. This may be due to the large thermal diffusivity along the field lines. The terminal effect and the response of wind are captured in all other simulations.

4 Summary and conclusions

In this study, we explore the application of the high-order numerical methods for ionosphere-plasmasphere modeling. Specifically, the nodal discontinuous Galerkin (DG) method is used to solve the dynamic equations (conservation laws with gravity and diffusion) along the magnetic field lines. A positive-definite integration scheme, the Patankar-Euler scheme, is used to solve the physical-chemical ODEs. A simple ExB drift model and semi-Lagrangian transport scheme are used for the perpendicular dynamics. The model uses the ragged array of variable length to better handle the varying number of points along different field lines. It also uses the MPI-IO for efficient parallel I/O.

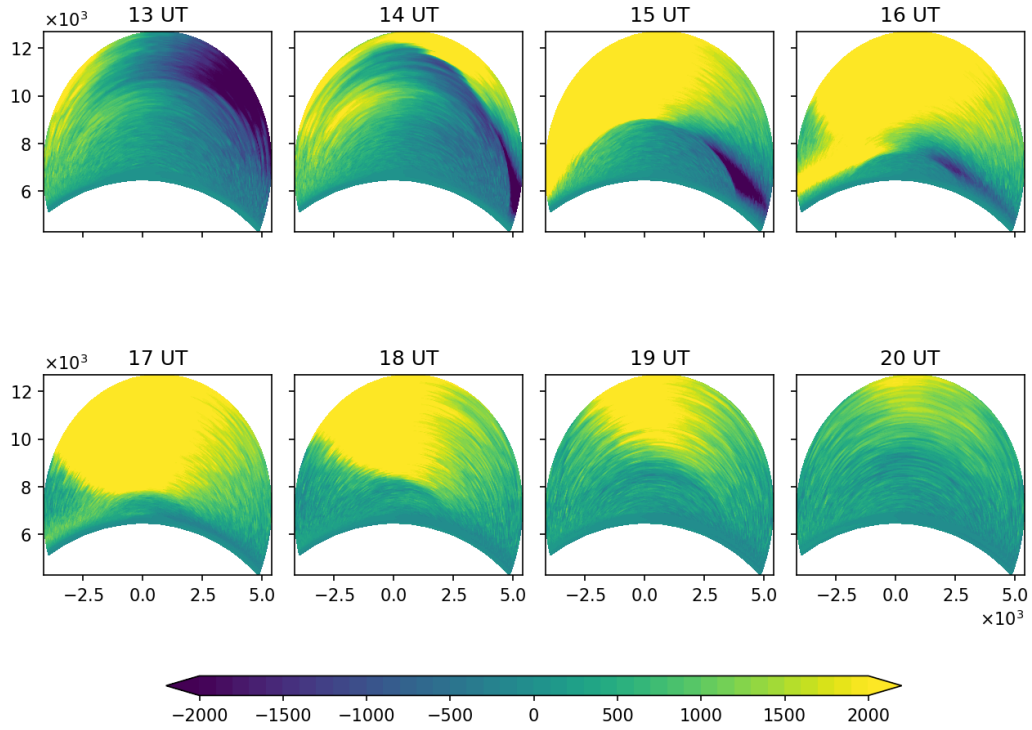

Figure 4. The meridional plane plot of the He^+ velocity [$m\,s^{-1}$] along the field line at the magnetic longitude 180°. The simulation results from the K101/N2 run are shown every hour from 13 to 20 UT, initialized at 00 UT on 21 March 2000. The geocentric x- and y-coordinates in [10^3 km] are used in the plot, with x from north to south.

The numerical simulations with different combinations of number of elements (K) and polynomial orders (N) show remarkable similarity. These *converging* results indicate the robustness of the algorithms and their implementation. The model also captures the dawn terminator effect very well as shown in the He^+ density field.

There are several areas that need to be explored for application of high-order numerical methods in ionosphere-plasmasphere modeling. The DG solver for ionospheric dynamo equation and conservative high-order transport schemes for ExB drift, such as the semi-Lagrangian discontinuous Galerkin (SLDG) scheme, will be the next step.

Appendix A Limiter, exponential filter and smoothness indicator

The choice and application of the limiters or filters are important to the success of the high-order DG methods. And the smoothness indicator can be used to decide where to apply the limiter or filter.

A1 The slope limiter

Limiter or reconstruction is one of the most important components for any successful implementation of high-order numerical methods. We discuss one of the limiters, the minmod slope limiter. First, define the minmod function

$$\text{minmod}(a_1,\ldots,a_m) = \begin{cases} s\min_{1\le i\le m}|a_i| & \text{if } |s|=1, \\ 0 & \text{otherwise,} \end{cases} \qquad s=\frac{1}{m}\sum_{i=1}^{m}\text{sign}(a_i). \tag{A1}$$

The minmod function returns the smallest of its arguments if all arguments have the same sign, otherwise it returns zero. Now define the interface fluxes as

$$v_l^k = \bar{u}_h^k - \text{minmod}(\bar{u}_h^k - u_l^k, \bar{u}_h^k - \bar{u}_h^{k-1}, \bar{u}_h^k - \bar{u}_h^{k+1}),$$
$$v_r^k = \bar{u}_h^k + \text{minmod}(u_r^k - \bar{u}_h^k, \bar{u}_h^k - \bar{u}_h^{k-1}, \bar{u}_h^k - \bar{u}_h^{k+1}),$$

where $\bar{u}_h^k$ is the cell average. Then, the slope limited solution is given by

$$\Pi^1 u_h^k(x) = \bar{u}_h^k + (x - x_0^k)\text{minmod}\left((u_h^k)_x, \frac{\bar{u}_h^k - \bar{u}_h^{k+1}}{h/2}, \frac{\bar{u}_h^k - \bar{u}_h^{k-1}}{h/2}\right),$$

where x_0^k is the center coordinate of D^k. In this study, the smoothness indicator is used to decide where to apply the limiter.

A2 Limiting the characteristic variables

When solving the hyperbolic system of conservation laws, more accurate results can be obtained if limiter is applied to the characteristic variables, instead of the conservative variables (e.g., Hesthaven, 2018). The characteristic variables can be derived as follows. The one-dimensional Euler equations can be written in quasilinear form as

$$\frac{\partial \boldsymbol{q}}{\partial t} + \mathcal{A}(\boldsymbol{q})\frac{\partial \boldsymbol{q}}{\partial x} = 0,$$

where $\boldsymbol{q}$ represents the conservative variables and $\mathcal{A}(\boldsymbol{q}) = \nabla_{\boldsymbol{q}} f$ is the Jacobian of the flux:

$$\boldsymbol{q} = \begin{bmatrix} \rho \\ \rho u \\ E \end{bmatrix}, \quad \mathcal{A}(\boldsymbol{q}) = \begin{bmatrix} 0 & 1 & 0 \\ -\frac{3-\gamma}{2}u^2 & (3-\gamma)u & \gamma - 1 \\ -\frac{\gamma E u}{\rho} + (\gamma-1)u^3 & \frac{\gamma E}{\rho} - \frac{3(\gamma-1)u^2}{2} & \gamma u \end{bmatrix}.$$

Matrix $\mathcal{A}$ can be diagonalized as

$$\boldsymbol{S}^{-1}\mathcal{A}\boldsymbol{S} = \boldsymbol{\Lambda} = \begin{bmatrix} u + c & 0 & 0 \\ 0 & u & 0 \\ 0 & 0 & u - c \end{bmatrix},$$

using

$$\boldsymbol{S} = \begin{bmatrix} \alpha & 1 & \alpha \\ \alpha(u + c) & u & \alpha(u - c) \\ \alpha(H + cu) & \frac{1}{2}u^2 & \alpha(H - cu) \end{bmatrix},$$

and

$$\boldsymbol{S}^{-1} = \begin{bmatrix} 2\alpha(\frac{1}{2}(\gamma-1)u^2 - cu) & -2\alpha((\gamma-1)u - c) & 2\alpha(\gamma-1) \\ 1 - \frac{1}{2}(\gamma-1)\frac{u^2}{c^2} & \frac{\gamma-1}{c^2}u & -\frac{\gamma-1}{c^2} \\ 2\alpha(\frac{1}{2}(\gamma-1)u^2 + cu) & -2\alpha((\gamma-1)u + c) & 2\alpha(\gamma-1) \end{bmatrix},$$

where we have introduced

$$\alpha = \frac{1}{2c}, \quad c = \sqrt{\frac{\gamma p}{\rho}}, \quad H = \frac{E + p}{\rho}$$

as a scaling constant, the speed of sound and the enthalpy, respectively.

To apply a limiter, the conservative variables $\boldsymbol{q}$ are transformed to the characteristics variables $\boldsymbol{R}$ by

$$\boldsymbol{R} = \boldsymbol{S}^{-1}\boldsymbol{q},$$

to which the limiter is applied. Then the limited characteristic variables $\tilde{\boldsymbol{R}}$ are transformed back to the conservative variables $\tilde{\boldsymbol{q}}$ by

$$\tilde{\boldsymbol{q}} = \boldsymbol{S}\tilde{\boldsymbol{R}},$$

which are the model state variables for the next time step. Since this needs to be done in every time step, it can be expensive to use.

A3 The exponential filter

The filter matrix of is defined by (e.g., Hesthaven & Warburton, 2008):

$$\mathcal{F} = \mathcal{V}\Lambda\mathcal{V}^{-1},$$

where $\mathcal{V}$ is the Vandermonde matrix and Λ is a diagonal matrix with entries

$$\Lambda_{ii} = \sigma\left(\frac{i-1}{N}\right), \quad i = 1, \ldots, N_p,$$

and the exponential filter defined by

$$\sigma(\eta) = \begin{cases} 1, & 0 \le \eta \le \eta_c = \frac{N_c}{N}, \\ \exp(-\alpha((\eta-\eta_c)/(1-\eta_c))^s), & \eta_c < \eta \le 1. \end{cases}$$

In this study, we choose the cutoff $N_c = 0$ and the maximum damping parameter $\alpha = 36$. The filter order s is even; increasing s would reduce filtering.

A4 The smoothness indicator

The smoothness indicator is defined by (Persson & Peraire, 2006; Ferrero & Larocca, 2016):

$$S_m = \frac{\int_{\mathsf{D}^k}(u_h^k - \tilde{u}_h^k)^2 dx}{\int_{\mathsf{D}^k}(u_h^k)^2 dx},$$

where

$$u_h^k(x,t) = \sum_{i=1}^{N_p} u_h^k(x_i^k,t)\ell_i^k(x), \quad \tilde{u}_h^k(x,t) = \sum_{i=1}^{N_p-1} u_h^k(x_i^k,t)\ell_i^k(x).$$

In practice, the logarithm of the smoothness indicator is used (Ferrero & Larocca, 2016):

$$S_I = \log_{10}(S_m).$$

Expecting S_m will scale like $1/N^4$, the smoothness threshold (S_R) of the following form is used:

$$S_R = \log_{10}(C_R/N^4) = \log_{10}(C_R) - 4\log_{10}(N),$$

where $N = N_p - 1$ is the order of polynomials used in the solutions, thus leaving the constant C_R as the only parameter to be adjusted according to the problem at hand.

Appendix B Thermal conductivity and collisional frequency

We summarize computation of thermal conductivity and collisional frequency as used in the SAMI2 model (Huba et al., 2000). Fortran code for computing the physical and chemical forcing terms is extracted from SAMI2 open source code (`https://github.com/NRL-Plasma-Physics-Division/SAMI2`) and modified for the current model.

B1 Thermal conductivity

The thermal conductivities κ_i and κ_e [$\mathrm{eV\,cm^{-1}\,s^{-1}\,K^{-1}}$] of the ith ion and electrons are given by (Banks & Kockarts, 1973; Bailey & Balan, 1996)

$$\kappa_i = 4.6 \times 10^4 \frac{n_i T_i^{5/2}}{n_e A_i^{1/2}},$$

where A_i is the ion mass in [a.m.u.], and

$$\kappa_e = \frac{7.7 \times 10^5 T_e^{5/2}}{1 + 3.22 \times 10^4 T_e^2 N_q / n_e},$$

where

$$N_q = 1.10\times10^{-16}n[\mathrm{O}](1+5.7\times10^{-4}T_e) + 2.82\times10^{-17}n[\mathrm{N_2}](1-1.2\times10^{-4}T_e)T_e^{1/2} + 2.20\times10^{-16}n[\mathrm{O_2}](1+3.6\times10^{-2}T_e^{1/2}).$$

B2 The ion-ion collision frequency

The ion-ion collision frequency ν_{ij} in [s^{-1}] is given by

$$\nu_{ij} = 9.2\times10^{-2}n_j\lambda_{ij}\frac{A_j^{1/2}}{A_i}\left(1+\frac{A_j}{A_i}\right)^{-1/2}\frac{1}{T^{3/2}},$$
$$\lambda_{ij} = 23-\ln\left[\frac{A_i+A_j}{A_iT_j+A_jT_i}\left(\frac{n_i}{T_i}+\frac{n_j}{T_j}\right)^{1/2}\right].$$

where A_i and A_j are the atomic ion mass in [a.m.u.], T is in [eV], and n_j in [cm^{-3}]. Temperature is converted from [K] to [eV] by

$$T_{eV} = 8.6174\times10^{-5}T_K.$$

B3 The ion-neutral collision frequency

The ion-neutral collision frequency ν_{in} in [s^{-1}] is given by

$$\nu_{in} = \frac{m+n}{m_i+m_n}\bar{\nu}_{in}, \tag{B1}$$
$$\bar{\nu}_{in} = 2.69\times10^{-9}\frac{\alpha_0 n_n}{\mu_A^{1/2}},$$
$$\mu_A = \frac{A_iA_n}{A_i+A_n},$$

where α_0 is the polarizability. Several temperature-dependent ion-neutral collision frequencies (Bailey & Balan, 1996) are used in place of (B1):

$$\nu_{\mathrm{H^+O}} = 6.61\times10^{-11}n[\mathrm{O}]T^{1/2}(1.00-0.047\log_{10}T)^2, \quad T=T_{\mathrm{H^+}},$$
$$\nu_{\mathrm{O^+O}} = 4.45\times10^{-11}n[\mathrm{O}]T^{1/2}(1.04-0.067\log_{10}T)^2, \quad T=(T_{\mathrm{O^+}}+T_n)/2,$$
$$\nu_{\mathrm{O_2^+O_2}} = 2.59\times10^{-11}n[\mathrm{O_2}]T^{1/2}(1.00-0.073\log_{10}T)^2, \quad T=(T_{\mathrm{O_2^+}}+T_n)/2,$$
$$\nu_{\mathrm{N_2^+N_2}} = 5.14\times10^{-11}n[\mathrm{N_2}]T^{1/2}(1.00-0.069\log_{10}T)^2, \quad T=(T_{\mathrm{N_2^+}}+T_n)/2,$$

where the temperature is in [K] and the number density of the neutrals is in [cm^{-3}].

B4 The electron-neutral collisional heating

The electron-neutral heating term (7d) can be written as

$$Q_{en} = \frac{2}{3}\sum_q\frac{m_em_q}{(m_e+m_q)^2}\nu_{eq}[3(T_q-T_e)],$$
$$= \frac{2}{3}\sum_q\bar{\nu}_{eq}(T_q-T_e),$$

where $\bar{\nu}_{eq}$ denotes the effective heating rate. The elastic electron-neutral collisional heating rates are given by (Banks & Kockarts, 1973):

$$\bar{\nu}_{e\mathrm{N_2}} = 1.2\times10^{-19}n[\mathrm{N_2}](1-1.2\times10^{-4}T_e)T_e,$$
$$\bar{\nu}_{e\mathrm{O_2}} = 7.9\times10^{-19}n[\mathrm{O_2}](1-3.6\times10^{-2}T_e^{1/2})T_e^{1/2},$$
$$\bar{\nu}_{e\mathrm{O}} = 7.2\times10^{-18}n[\mathrm{O}]T_e^{1/2},$$
$$\bar{\nu}_{e\mathrm{H}} = 6.3\times10^{-16}n[\mathrm{H}](1-1.35\times10^{-4}T_e)T_e^{1/2}.$$

The units are collisional heating rates [$\mathrm{eV\,K^{-1}\,s^{-1}}$], the temperature [K] and the number density [$\mathrm{cm^{-3}}$].

B5 The photoelectron heating

At altitudes lower than 300 km, the photoelectron heating rate [$\mathrm{eV\,s^{-1}}$] is computed from

$$
\begin{aligned}
Q_{\mathrm{phe}} &= \frac{2}{3}\frac{1}{n_e}\epsilon P_{\mathrm{photo}},\\
\epsilon &= \exp[-p(x)],\\
p(x) &= 12.75 + 6.94x + 1.66x^2 + 0.08034x^3 + 0.001996x^4,\\
x &= \ln\left(\frac{n_e}{n[\mathrm{O_2}] + n[\mathrm{N_2}] + 0.1n[\mathrm{O}]}\right),
\end{aligned}
$$

where P_{photo} is the total photoionization rate. At altitudes higher than 300 km, the photoelectron heating rate is computed as

$$
Q_{\mathrm{phe}}(\ell) = \frac{2}{3}\frac{B(\ell)}{B(\ell_{300})}Q_{\mathrm{phe}}(\ell_{300})\exp\left(-C_{qe}\int_{\ell_{300}}^{\ell} n_e d\ell\right),
$$

where B is the magnetic field strength, the constant C_{qe} is taken to be 7.0×10^{-14} $\mathrm{cm^2}$, and the integration along the flux tube is from both hemispheres.

References

Anderson, E., Bai, Z., Bischof, C., Blackford, S., Demmel, J., Dongarra, J., ... Sorensen, D. (1999). *LAPACK Users' Guide* (Third ed.). Philadelphia, PA: Society for Industrial and Applied Mathematics.

Bailey, G. J., & Balan, N. (1996). A low-latitude ionosphere-plasmasphere model. In R. W. Schunk (Ed.), *Handb. ionos. model.* (pp. 173–206).

Banks, P. M., & Kockarts, G. (1973). *Aeronomy, Part B.* New York: Elsevier. doi: 10.1016/C2013-0-10329-7

Bilitza, D. (2018). IRI the international standard for the ionosphere. *Adv. Radio Sci.*, *16*, 1–11. doi: 10.5194/ars-16-1-2018

Burchard, H., Deleersnijder, E., & Meister, A. (2003). A high-order conservative Patankar-type discretisation for stiff systems of production-destruction equations. *Appl. Numer. Math.*, *47*(1), 1–30. doi: 10.1016/S0168-9274(03)00101-6

Cai, X., Guo, W., & Qiu, J.-M. (2017). A high order conservative semi-Lagrangian discontinuous Galerkin method for two-dimensional transport simulations. *J. Sci. Comput.*, *73*(2-3), 514–542. doi: 10.1007/s10915-017-0554-0

Canuto, C., Hussaini, M. Y., Quarteroni, A., & Zang, T. A. (2006). *Spectral Methods: Fundamentals in Single Domains.* Berlin, Heidelberg: Springer Berlin Heidelberg. doi: 10.1007/978-3-540-30726-6

Cockburn, B., Karniadakis, G. E., & Shu, C.-W. (2000). The Development of Discontinuous Galerkin Methods. In B. Cockburn, G. E. Karniadakis, & C.-W. Shu (Eds.), *Discontinuous galerkin methods* (pp. 3–50). Springer, Berlin, Heidelberg. doi: 10.1007/978-3-642-59721-3_1

Courant, R., Friedrichs, K., & Lewy, H. (1967). On the partial difference equations of mathematical physics. *IBM J. Res. Dev.*, *11*(2), 215–234. doi: 10.1147/rd.112.0215

Denton, M. H., Bailey, G. J., Wilford, C. R., Rodger, A. S., & Venkatraman, S. (2002). He^+ dominance in the plasmasphere during geomagnetically disturbed periods: 1. Observational results. *Ann. Geophys.*, *20*(4), 461–470. doi: 10.5194/angeo-20-461-2002

Deville, M. O., Fischer, P. F., & Mund, E. H. (2002). *High-Order Methods for Incompressible Fluid Flow*. Cambridge University Press. doi: 10.1017/cbo9780511546792

Fazio, R., & Jannelli, A. (2010). Second order numerical operator splitting for 3D advection–diffusion-reaction models. In *Numer. math. adv. appl. 2009* (pp. 317–324). Berlin, Heidelberg: Springer Berlin Heidelberg. doi: 10.1007/978-3-642-11795-4_33

Fejer, B. G., Souza, J. R., Santos, A. S., & Costa Pereira, A. E. (2005). Climatology of F region zonal plasma drifts over Jicamarca. *J. Geophys. Res. Sp. Phys.*, *110*(A12), 12310. doi: 10.1029/2005JA011324

Ferrero, A., & Larocca, F. (2016). Feedback filtering in discontinuous Galerkin methods for Euler equations. *Prog. Comput. Fluid Dyn. An Int. J.*, *16*(1), 14. doi: 10.1504/PCFD.2016.074221

Giraldo, F., & Restelli, M. (2008). A study of spectral element and discontinuous Galerkin methods for the Navier–Stokes equations in nonhydrostatic mesoscale atmospheric modeling: Equation sets and test cases. *J. Comput. Phys.*, *227*(8), 3849–3877. doi: 10.1016/j.jcp.2007.12.009

Gottlieb, S., Shu, C. W., & Tadmor, E. (2001). Strong stability-preserving high-order time discretization methods. *SIAM Rev.*, *43*(1), 89–112. doi: 10.1137/S003614450036757X

Gropp, W., Hoefler, T., Thakur, R., & Lusk, E. (2014). *Using Advanced MPI: Modern Features of the Message-Passing Interface*. The MIT Press.

Gustafsson, B. (2008). *High Order Difference Methods for Time Dependent PDE* (Vol. 38). Berlin, Heidelberg: Springer Berlin Heidelberg. doi: 10.1007/978-3-540-74993-6

Hain, K. H. (1987). The partial donor cell method. *J. Comput. Phys.*, *73*(1), 131–147. doi: 10.1016/0021-9991(87)90110-0

Hedin, A. E. (1987). MSIS-86 thermospheric model. *J. Geophys. Res.*, *92*(A5), 4649. doi: 10.1029/ja092ia05p04649

Hedin, A. E., Biondi, M. A., Burnside, R. G., Hernandez, G., Johnson, R. M., Killeen, T. L., ... Virdi, T. S. (1991). Revised global model of thermosphere winds using satellite and ground-based observations. *J. Geophys. Res.*, *96*(A5), 7657. doi: 10.1029/91ja00251

Hesthaven, J. S. (2018). *Numerical Methods for Conservation Laws: From Analysis to Algorithms*. Philadelphia, PA: Society for Industrial and Applied Mathematics. doi: 10.1137/1.9781611975109

Hesthaven, J. S., & Warburton, T. (2008). *Nodal Discontinuous Galerkin Methods* (Vol. 54). New York, NY: Springer New York. doi: 10.1007/978-0-387-72067-8

Huba, J. D. (2003). Hall Magnetohydrodynamics - A Tutorial. In *Sp. plasma simul.* (pp. 166–192). Berlin, Heidelberg: Springer Berlin Heidelberg. doi: 10.1007/3-540-36530-3_9

Huba, J. D., Joyce, G., & Fedder, J. A. (2000). Sami2 is Another Model of the Ionosphere (SAMI2): A new low-latitude ionosphere model. *J. Geophys. Res.*, *105*.

Huba, J. D., & Liu, H. L. (2020). Global Modeling of Equatorial Spread F with SAMI3/WACCM-X. *Geophys. Res. Lett.*, *47*(14). doi: 10.1029/2020GL088258

Mitra, A. P. (1968). A review of D-region processes in non-polar latitudes. *J. Atmos. Terr. Phys.*, *30*(6), 1065–1114. doi: 10.1016/S0021-9169(68)90606-5

Patankar, S. V. (1980). *Numerical Heat Transfer and Fluid Flow*. CRC Press. doi: 10.1201/9781482234213

Persson, P. O., & Peraire, J. (2006). Sub-cell shock capturing for discontinuous Galerkin methods. In *44th aiaa aerosp. sci. meet.* (Vol. 2, pp. 1408–1420). doi: 10.2514/6.2006-112

Proft, J., & Rivière, B. (2009). Discontinuous Galerkin methods for convection-diffusion equations for varying and vanishing diffusivity. *Int. J. Numer. Anal.*

Model., *6*(4), 533–561.

Scherliess, L., & Fejer, B. (1999). Radar and satellite global equatorial F region vertical model. *J. Geophys. Res.*, *104*, 6829–6842.

Schunk, R., & Nagy, A. (2009). *Ionospheres: Physics, Plasma Physics, and Chemistry* (2nd ed.). Cambridge University Press. doi: 10.1017/CBO9780511635342

Schunk, R. W. (Ed.). (1996). *Handbook of Ionospheric Models*. SCOSTEP. Retrieved from `https://www.bc.edu/content/dam/bc1/offices/ISR/SCOSTEP/Multimedia/other/ionospheric-models.pdf`

Shahbazi, K. (2005). An explicit expression for the penalty parameter of the interior penalty method. *J. Comput. Phys.*, *205*(2), 401–407. doi: 10.1016/j.jcp.2004.11.017

Strang, G. (1968). On the Construction and Comparison of Difference Schemes. *SIAM J. Numer. Anal.*, *5*(3), 506–517. doi: 10.1137/0705041

Wang, H. (2021). A general curvilinear magnetic field-line-following coordinate system for ionosphere-plasmasphere modeling. *Earth Sp. Sci. Open Arch.*, 13. doi: 10.1002/essoar.10508238.1

Wilford, C. R., Moffett, R. J., Rees, J. M., Bailey, G. J., & Gonzalez, S. A. (2003). Comparison of the He+ layer observed over Arecibo during solar maximum and solar minimum with CTIP model results. *J. Geophys. Res. Sp. Phys.*, *108*(A12), 1452. doi: 10.1029/2003JA009940

Zettergren, M., & Semeter, J. (2012). Ionospheric plasma transport and loss in auroral downward current regions. *J. Geophys. Res.*, *117*(A6), A06306. doi: 10.1029/2012JA017637